

# Mid-infrared spectrally-uncorrelated biphotons generation from doped PPLN: a theoretical investigation

Bei Wei<sup>1,a</sup>, Wu-Hao Cai<sup>1,a</sup>, Chunling Ding<sup>1</sup>, Guang-Wei Deng<sup>2,3,\*</sup>, Ryosuke Shimizu<sup>4</sup>, Qiang Zhou<sup>2,3,†</sup> and Rui-Bo Jin<sup>1,5‡</sup>  
<sup>1</sup>Hubei Key Laboratory of Optical Information and Pattern Recognition,  
Wuhan Institute of Technology, Wuhan 430205, PR China

<sup>2</sup>Institute of Fundamental and Frontier Sciences and School of Optoelectronic Science and Engineering,  
University of Electronic Science and Technology of China, Chengdu 610054, China

<sup>3</sup>CAS Key Laboratory of Quantum Information, University of Science and Technology of China, Hefei 230026, China

<sup>4</sup>The University of Electro-Communications, 1-5-1 Chofugaoka, Chofu, Tokyo, Japan

<sup>5</sup>State Key Laboratory of Quantum Optics and Quantum Optics Devices, Shanxi University, Taiyuan, 030006, China and

<sup>a</sup>These authors contributed equally to this work

(Dated: December 18, 2020)

We theoretically investigate the preparation of mid-infrared (MIR) spectrally-uncorrelated biphotons from a spontaneous parametric down-conversion process using doped LN crystals, including MgO doped LN, ZnO doped LN, and In<sub>2</sub>O<sub>3</sub> doped ZnLN with doping ratio from 0 to 7 mol%. The tilt angle of the phase-matching function and the corresponding poling period are calculated under type-II, type-I, and type-0 phase-matching conditions. We also calculate the thermal properties of the doped LN crystals and their performance in Hong-Ou-Mandel interference. It is found that the doping ratio has a substantial impact on the group-velocity-matching (GVM) wavelengths. Especially, the GVM<sub>2</sub> wavelength of co-doped InZnLN crystal has a tunable range of 678.7 nm, which is much broader than the tunable range of less than 100 nm achieved by the conventional method of adjusting the temperature. It can be concluded that the doping ratio can be utilized as a degree of freedom to manipulate the biphoton state. The spectrally uncorrelated biphotons can be used to prepare pure single-photon source and entangled photon source, which may have promising applications for quantum-enhanced sensing, imaging, and communications at the MIR range.

## I. INTRODUCTION

The mid-infrared (MIR) wavelength range (approximately 2-20  $\mu\text{m}$ ) is of great interest to a variety of scientific and technological applications in sensing, imaging, and communications [1, 2]. Firstly, this range contains strong absorption bands of a variety of gases, leads to essential applications in gas sensing [3] and environmental monitoring [4]. Secondly, the MIR region covers the atmospheric transmission window between 3  $\mu\text{m}$  and 5  $\mu\text{m}$ . This region with relatively high transparency is beneficial for atmospheric monitoring and free-space communications [5]. Thirdly, room temperature objects emit light at MIR wavelengths, resulting in novel applications in infrared thermal imaging [6, 7]. Fourthly, with the rapid development of optical fiber communications, there is a growing demand to expand the communication wavelengths into the MIR region to increase the communication bandwidth [8].

All these practical applications mentioned above are based on strong light sources in the MIR region. However, the advantages of the MIR range have not been fully exploited using quantum technology. In order to further improve the sensitivity in those applications, one promising approach is to utilize a single-photon source

or entangled photon source in the MIR region. Spontaneous parametric down-conversion (SPDC) is one of the widely used methods to prepare biphotons, which can be used to produce single-photon source and entangled photon source. Previously, several theoretical and experimental works have been dedicated to the development of single or entangled photon source in MIR range from an SPDC process. In 2016, Lee et al. calculated the extended phase-matching properties of periodically poled potassium niobate (PPKN) for single-photon generation at the MIR range [9]. In 2017, Mancinelli et al. performed coincidence measurements on twin photons generated from periodically poled lithium niobate (PPLN) at 3.1  $\mu\text{m}$  [7]. In 2018, McCracken, et al. numerically investigated the mid-infrared single-photon generation in a range of novel nonlinear materials, including PPLN, PPKTP, GaP, GaAs, CdSiP<sub>2</sub>, and ZnGeP<sub>2</sub> [10]. In 2019, Rosenfeld et al. experimentally prepared MIR photon pairs in a four-wave mixing process from a silicon-on-insulator waveguide at around 2.1  $\mu\text{m}$  [11]. In 2020 Kundys et al. numerically studied the reconfigurable MIR single-photon sources based on functional ferroelectrics, i.e., PMN-0.38PT crystal at 5.6  $\mu\text{m}$  [12]. In the same year, Prabhakar et al. experimentally demonstrated the entangled photons generation and Hong-Ou-Mandel interference at 2.1  $\mu\text{m}$  from PPLN crystals [13].

Many biphoton sources have been demonstrated in the previous studies [7, 9, 10, 12, 13]; however, from the experimental point of view, it is still lack of high-quality biphotons source at the MIR range, especially the spec-

\* gwdeng@uestc.edu.cn

† zhouqiang@uestc.edu.cn

‡ jrbqyj@gmail.com

trally uncorrelated biphotons [14–18]. The biphotons generated from an SPDC process are generally spectrally correlated due to the energy and momentum conservation laws. However, it is necessary to utilize biphotons with no spectral correlations to obtain the heralded pure-state single photon for many quantum information processing (QIP) protocols, such as quantum computation [19], boson sampling [20], and quantum teleportation [21], measurement-device-independent quantum key distribution [22]. In quantum sensing, a high-NOON state, which provides high accuracy for phase-sensitive measurements, should be prepared from spectrally uncorrelated biphotons [23, 24]. Therefore, spectral uncorrelation of photon pairs from SPDC is indispensable for the future development of quantum information at the MIR range.

In this work, we investigate the generation of spectrally uncorrelated biphotons from PPLN crystals at MIR range. PPLN has the merits of large nonlinear coefficient and wide transparency range ( $0.4 \mu\text{m} \sim 5 \mu\text{m}$ ) [25–28]. Another unique advantage of PPLN is that its intrinsic group-velocity-matched (GVM) wavelengths are in the MIR range, and the spectrally uncorrelated biphoton state can be engineered at the GVM wavelengths [14, 29].

In addition, we also consider the manipulation of the biphoton state by adding different dopants in PPLN. Traditionally, PPLN is doped with different dopants to improve its properties. For example, by doping Mg and Zr, the damage resistance can be improved from visible to ultraviolet region [30]; by doping Zn, the electro-optical coefficients can be improved [31]; by doping Fe, the photorefractive properties can be improved [32]. Especially, doping rare-earth elements (e.g., Tm, Er, Dy, Tb, Gd, Pr) makes PPLN a right candidate for lasers and quantum memories [33, 34]. It is natural to deduce that doping can also be utilized as a degree of freedom to manipulate the single photons state at the MIR range. Therefore, we study the spectrally uncorrelated biphotons generation from doped PPLN in this work. Specifically, we investigated the GVM wavelengths, the tilt angle, the poling period, the thermal properties and the HOM interferences of biphotons generated from three kinds of doped LN crystals, including MgLN [MgO( $x$  mol%)LiNbO<sub>3</sub>], ZnLN [ZnO( $x$  mol%)LiNbO<sub>3</sub>], and In-ZnLN [In<sub>2</sub>O<sub>3</sub>( $x$  mol%)ZnO(5.5 mol%)LiNbO<sub>3</sub>, with  $x$  from 0 to 7].

## II. THEORY

The biphoton state  $|\psi\rangle$  generated from SPDC can be expressed as [35]

$$|\psi\rangle = \int_0^\infty \int_0^\infty d\omega_s d\omega_i f(\omega_s, \omega_i) \hat{a}_s^\dagger(\omega_s) \hat{a}_i^\dagger(\omega_i) |0\rangle |0\rangle, \quad (1)$$

where  $\omega$  is the angular frequency,  $\hat{a}^\dagger$  is the creation operator, and the subscripts  $s$  and  $i$  indicate the signal and idler photon. The joint spectral amplitude

(JSA)  $f(\omega_s, \omega_i)$  can be calculated as the product of the pump envelope function (PEF)  $\alpha(\omega_s, \omega_i)$  and the phase-matching function (PMF)  $\phi(\omega_s, \omega_i)$ :

$$f(\omega_s, \omega_i) = \alpha(\omega_s, \omega_i) \times \phi(\omega_s, \omega_i). \quad (2)$$

A PEF with a Gaussian-distribution can be written as

$$\alpha(\omega_s, \omega_i) = \exp\left[-\frac{1}{2} \left(\frac{\omega_s + \omega_i - \omega_{p0}}{\sigma_p}\right)^2\right], \quad (3)$$

where  $\omega_{p0}$  is the center angular frequency of the pump;  $\sigma_p$  is the bandwidth of the pump, and the subscript  $p$  indicates the pump photon. The full-width at half-maximum (FWHM) is  $\text{FWHM}_\omega = 2\sqrt{\ln(2)}\sigma_p \approx 1.67\sigma_p$ .

If we choose wavelengths as the variables, the PEF can be rewritten as

$$\alpha(\lambda_s, \lambda_i) = \exp\left(-\frac{1}{2} \left\{ \frac{1/\lambda_s + 1/\lambda_i - 1/(\lambda_0/2)}{\Delta\lambda/[(\lambda_0/2)^2 - (\Delta\lambda/2)^2]} \right\}^2\right), \quad (4)$$

where  $\lambda_0/2$  is the central wavelength of the pump; The FWHM of the pump at intensity level is  $\text{FWHM}_\lambda = \frac{2\sqrt{\ln(2)}\lambda_0^2\Delta\lambda(\lambda_0^2 - \Delta\lambda^2)}{\lambda_0^4 + \Delta\lambda^4 - 2\lambda_0^2\Delta\lambda^2[1 + \ln(4)]}$ . For  $\Delta\lambda \ll \lambda_0$ ,  $\text{FWHM}_\lambda \approx 2\sqrt{\ln(2)}\Delta\lambda \approx 1.67\Delta\lambda$ .

The PMF function can be written as

$$\phi(\omega_s, \omega_i) = \text{Sinc}\left(\frac{\Delta k L}{2}\right), \quad (5)$$

where  $L$  is the length of the crystal,  $\Delta k = k_p - k_i - k_s \pm \frac{2\pi}{\Lambda}$  and  $k = \frac{2\pi n(\lambda)}{\lambda}$  is the wave vector.  $\Lambda$  is the poling period and can be calculated by

$$\Lambda = \frac{2\pi}{|k_p - k_i - k_s|}. \quad (6)$$

The angle  $\theta$  between the ridge direction of PMF and the horizontal axis is determined by [36]

$$\tan\theta = -\left(\frac{V_{g,p}^{-1}(\omega_p) - V_{g,s}^{-1}(\omega_s)}{V_{g,p}^{-1}(\omega_p) - V_{g,i}^{-1}(\omega_i)}\right), \quad (7)$$

where  $V_{g,\mu} = \frac{d\omega}{dk_\mu(\omega)} = \frac{1}{k'_\mu(\omega)}$ , ( $\mu = p, s, i$ ) is the group velocity. The shape of the JSA is determined by the following three GVM conditions [37, 38].

The GVM<sub>1</sub> condition ( $\theta = 0^\circ$ ):

$$V_{g,p}^{-1}(\omega_p) = V_{g,s}^{-1}(\omega_s). \quad (8)$$

The GVM<sub>2</sub> condition ( $\theta = 90^\circ$ ):

$$V_{g,p}^{-1}(\omega_p) = V_{g,i}^{-1}(\omega_i). \quad (9)$$

The GVM<sub>3</sub> condition ( $\theta = 45^\circ$ ):

$$2V_{g,p}^{-1}(\omega_p) = V_{g,s}^{-1}(\omega_s) + V_{g,i}^{-1}(\omega_i). \quad (10)$$

The purity can be calculated by performing Schmidt decomposition on  $f(\omega_s, \omega_i)$ :

$$f(\omega_s, \omega_i) = \sum_j c_j \phi_j(\omega_s) \varphi_j(\omega_i), \quad (11)$$

where  $\phi_j(\omega_s)$  and  $\varphi_j(\omega_i)$  are the two orthogonal basis vectors in the frequency domain, and  $c_j$  is a set of non-negative real numbers that satisfy the normalization condition  $\sum_j c_j^2 = 1$ . The purity  $p$  is defined as:

$$p = \sum_j c_j^4. \quad (12)$$

GVM wavelengths are important parameters for nonlinear crystals. The maximal purities under GVM<sub>1</sub>, GVM<sub>2</sub>, and GVM<sub>3</sub> conditions are around 0.97, 0.97, and 0.82, respectively [37].

Note the three GVM conditions in Eqs.(8-10) are also called fully-asymmetric GVM or symmetric GVM conditions in Ref. [17]. In fact, the spectrally-pure state can be prepared for any  $\theta$  angle between 0 and 90 degrees, independently from the PDC-type (type-0, type-I, or type-II) and wavelength degeneracy (degenerated or non-degenerated). Perfectly separable JSA can be achieved only with Gaussian pump and Gaussian PMF (via domain engineering techniques), as proven in Ref. [39]. However, the three GVM conditions listed in Eqs.(8-10) with the degenerated wavelengths are the most widely used cases in the experiments [40–42]. Especially, the GVM<sub>3</sub> condition has a symmetric distribution along the anti-diagonal direction, i.e.,  $f(\omega_s, \omega_i) = f(\omega_i, \omega_s)$ , which is the prerequisite condition for high-visibility HOM interferences. Therefore, we mainly focus on the type-II phase-matching condition in the calculation below.

### III. CALCULATION AND SIMULATION

In this section, we first calculate the angle  $\theta$  in the range of 0 and 90 degrees, and the corresponding poling period  $\Lambda$  under type-II, type-I, and type-0 phase-matching conditions. Then, we consider the thermal properties, and the HOM interferences for the doped PPLN crystals under the type-II phase-matching condition. The Sellmeier equations for these crystals are chosen from Refs. [43–45], where the Sellmeier equations are parameterized by the dopant concentration. The PPLN crystals are negative uniaxial crystals ( $n_o > n_e$ ), where  $n_{o(e)}$  is the refractive index of the ordinary (extraordinary) ray.

#### A. Angle $\theta$ and poling period $\Lambda$ for type-II phase-matching condition

In the calculation below, we consider type-II phase-matched ( $o \rightarrow o + e$ ) SPDC in a collinear configuration

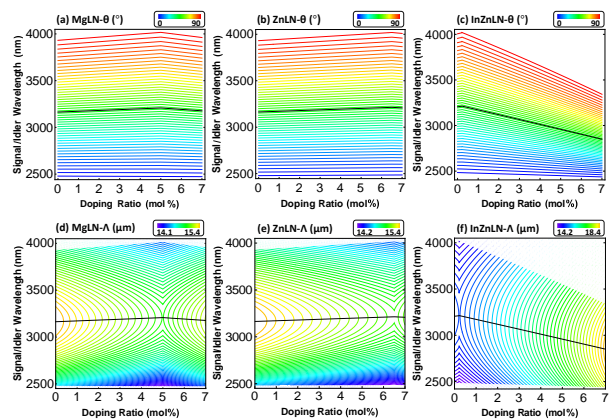


FIG. 1. (a-c): The tilt angle  $\theta$  as a function of signal (idler) wavelength and doping ratio  $x$  for MgLN [ $\text{MgO}(x \text{ mol}\%):\text{LiNbO}_3$ ], ZnLN [ $\text{ZnO}(x \text{ mol}\%):\text{LiNbO}_3$ ], and InZnLN [ $\text{In}_2\text{O}_3(x \text{ mol}\%):\text{ZnO}(5.5 \text{ mol}\%):\text{LiNbO}_3$ ]. (d-f): The corresponding poling period. In these figures, the signal and the idler photons have degenerated wavelengths under the **type-II** phase-matching condition. The solid black line indicates  $\theta = 45^\circ$ .

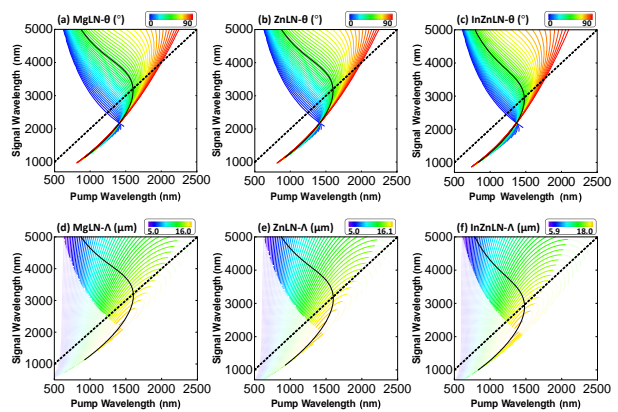


FIG. 2. (a-c): The tilt angle  $\theta$  as functions of the signal wavelength and the pump wavelength for crystals with fixed doping ratio, i.e., MgLN [ $\text{MgO}(5 \text{ mol}\%):\text{LiNbO}_3$ ], ZnLN [ $\text{ZnO}(5 \text{ mol}\%):\text{LiNbO}_3$ ], and InZnLN [ $\text{In}_2\text{O}_3(5 \text{ mol}\%):\text{ZnO}(5.5 \text{ mol}\%):\text{LiNbO}_3$ ]. (d-f): The corresponding poling period. In these figures, the signal and the idler photons have the non-degenerated wavelengths under the **type-II** phase-matching condition. The solid black line indicates  $\theta = 45^\circ$ , and the dashed black line indicates  $\lambda_s = 2\lambda_p$ .

with wavelength degenerated ( $2\lambda_p = \lambda_s = \lambda_i$ ) or non-degenerated ( $\lambda_s \neq \lambda_i$ ). In the type-II phase-matching condition, we set the pump and the signal as o-ray, and the idler as e-ray. Figure 1(a-c) shows the tilt angle  $\theta$  as a function of the doping ratio ( $x \text{ mol}\%$ ) and signal/idler (degenerated) wavelength. For MgLN in Fig. 1(a), on the line of  $\theta = 0^\circ$ , the GVM<sub>1</sub> wavelength increased monotonically, i.e., from 2478.6 nm at  $x = 0$  to 2472.7 nm at  $x = 7$ . For  $\theta = 90^\circ$ , the GVM<sub>2</sub> wavelength increased non-monotonically from 3931.4 nm ( $x = 0$ ) to the maximal value of 4016.6 nm ( $x = 5$ ), and then decreased to 3961.6

nm ( $x = 7$ ). For  $\theta = 45^\circ$ , the GVM<sub>3</sub> wavelength also increased non-monotonically, i.e., increased from 3163.6 nm ( $x = 0$ ) to 3207.6 nm ( $x = 5$ ), and then decreased to 3177.1 nm ( $x = 7$ ).

For ZnLN in Fig. 1(b), on the line of  $\theta = 0^\circ$ , the GVM<sub>1</sub> wavelength increased monotonically from 2478.6 nm at  $x = 0$  to 2485.8 nm at  $x = 7$ . On the line of  $\theta = 90^\circ$ , the GVM<sub>2</sub> wavelength start from 3931.4 nm at  $x = 0$ , and reach a maximal value of 4019.3 nm at  $x = 6.5$ , and then decreased to 4009.0 nm at  $x = 7$ . On the line of  $\theta = 45^\circ$ , the GVM<sub>3</sub> wavelength is 3163.6 nm, 3213.6 nm, and 3208.2 nm, at  $x = 0, 6.5$ , and 7, respectively.

Crystal Name	MgLN	ZnLN	InZnLN
$\lambda_{\text{GVM1}}$ at 0 mol% (nm)	2478.6	2478.6	2484.3
$\lambda_{\text{GVM1}}$ at 7 mol% (nm)	2472.7	2485.8	2436.9
$\Delta\lambda_{\text{GVM1}}$ (nm)	5.9	-7.2	47.4
$\lambda_{\text{GVM2}}$ at 0 mol% (nm)	3931.4	3931.4	4006.0
$\lambda_{\text{GVM2}}$ at 7 mol% (nm)	3961.6	4009.0	3342.9
Maximum of $\lambda_{\text{GVM2}}$	4016.6	4019.3	4021.6
$\Delta\lambda_{\text{GVM2}}$ (nm)	-85.2	-87.9	678.7
$\lambda_{\text{GVM3}}$ at 0 mol% (nm)	3163.6	3163.6	3205.9
$\lambda_{\text{GVM3}}$ at 7 mol% (nm)	3177.1	3208.2	2850.4
Maximum of $\lambda_{\text{GVM3}}$	3207.6	3213.6	3213.9
$\Delta\lambda_{\text{GVM3}}$ (nm)	-44.0	-50.0	363.5

TABLE I. Summary of the GVM wavelengths in Fig.1 at different doping ratios. The maximal  $\lambda_{\text{GVM}}$  is achieved at the doping ratio of 5 mol% for MgLN, 6.5 mol% for ZnLN, and 0.2 mol% for InZnLN.  $\Delta\lambda$  is the maximal difference of the GVM wavelengths.

For InZnLN in Fig. 1(c), the GVM<sub>1</sub> ( $\theta = 0$ ) wavelength decreased monotonically from 2484.3 nm at  $x = 0$  to 2436.9 nm at  $x = 7$ . The GVM<sub>2</sub> ( $\theta = 90^\circ$ ) wavelength increased non-monotonically: start from 4006.0 nm at  $x = 0$  and reach a maximal value of 4021.6 nm at  $x = 0.2$ , and then decreased to 3342.9 nm at  $x = 7$ . The GVM<sub>3</sub> ( $\theta = 45^\circ$ ) wavelength also increased non-monotonically, the wavelengths are 3205.9 nm, 3213.9 nm, and 2850.4 nm at  $x = 0, 0.2$ , and 7, respectively. Figure 1(d-f) shows the poling period for each crystal.  $\Lambda$  is 14.1  $\mu\text{m}$  to 15.4  $\mu\text{m}$  for MgLN, 14.2  $\mu\text{m}$  to 15.4  $\mu\text{m}$  for ZnLN, and 14.2  $\mu\text{m}$  to 18.4  $\mu\text{m}$  for InZnLN. For comparison, we also list the wavelength of GVM<sub>1</sub>, GVM<sub>2</sub>, and GVM<sub>3</sub> at different doping ratios in Tab.I. It can be discovered in Tab.I that the co-doped crystal, InZnLN, has a large tunable wavelength range of 678.7 nm. This feature is essential for quantum state engineering at the MIR wavelength range.

Next, we consider the wavelength non-degenerated cases for a fixed doping ratio, i.e., MgO(5 mol%):LiNbO<sub>3</sub>, ZnO(5 mol%):LiNbO<sub>3</sub>, and In<sub>2</sub>O<sub>3</sub>(5 mol%):ZnO(5.5 mol%):LiNbO<sub>3</sub>. Figure 2(a-c) shows the angle  $\theta$  as a function of the pump and the signal wavelengths for MgLN, ZnLN, InZnLN, with the same doping ratio of 5 mol%. On the line of  $\theta = 0^\circ$  ( $\theta = 90^\circ$ ), the signal wavelength decreases (increases) monotonically with the increase of the pump wavelength. On the line of  $\theta = 45^\circ$ ,

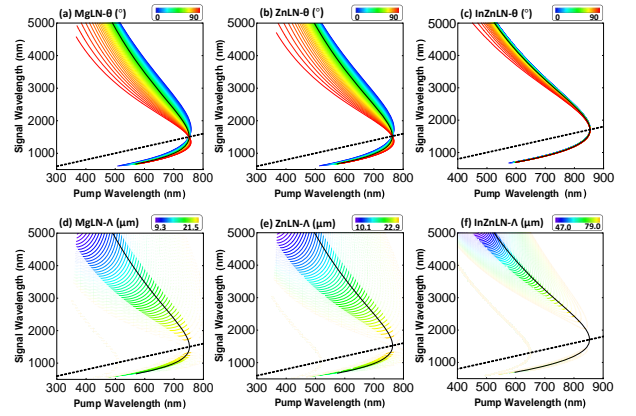


FIG. 3. (a-c): The tilt angle  $\theta$  as a function of the signal wavelength and the pump wavelength for crystals with fixed doping ratio, i.e., MgLN [MgO(5 mol%):LiNbO<sub>3</sub>], ZnLN [ZnO(5 mol%):LiNbO<sub>3</sub>], and InZnLN [In<sub>2</sub>O<sub>3</sub>(5 mol%):ZnO(5.5 mol%):LiNbO<sub>3</sub>]. (d-f): The corresponding poling period. In these figures, the signal and the idler photons have the non-degenerated wavelengths under **type-I** phase-matching condition. The solid black line indicates  $\theta = 45^\circ$ , and the dashed black line indicates  $\lambda_s = 2\lambda_p$ .

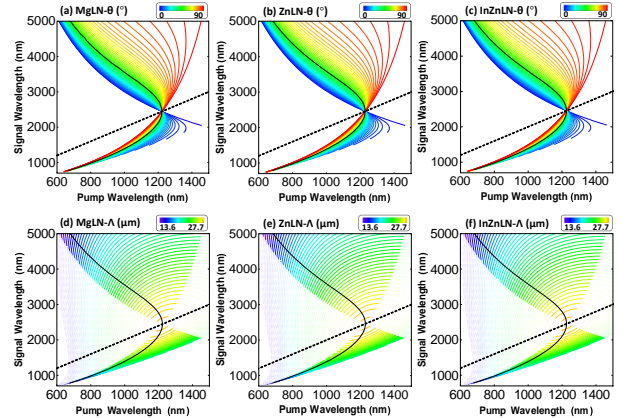


FIG. 4. (a-c): The tilt angle  $\theta$  as functions of the signal wavelength and the pump wavelength for crystals with fixed doping ratio, i.e., MgLN [MgO(5 mol%):LiNbO<sub>3</sub>], ZnLN [ZnO(5 mol%):LiNbO<sub>3</sub>], and InZnLN [In<sub>2</sub>O<sub>3</sub>(5 mol%):ZnO(5.5 mol%):LiNbO<sub>3</sub>]. (d-f): The corresponding poling period. In these figures, the signal and the idler photons have the non-degenerated wavelengths under **type-0** phase-matching condition. The solid black line indicates  $\theta = 45^\circ$ , and the dashed black line indicates  $\lambda_s = 2\lambda_p$ .

the signal wavelength changes non-monotonically. Figure 2(d-f) shows the corresponding poling period  $\Lambda$ , ranging from 5.0  $\mu\text{m}$  to 18.0  $\mu\text{m}$  for the three crystals.

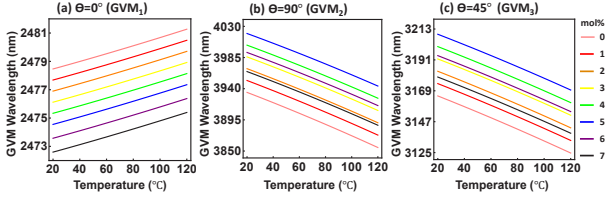


FIG. 5. Three GVM wavelengths of MgLN [ $\text{MgO}(x \text{ mol\%})\text{:LiNbO}_3$ ] with different doping ratio  $x$  (mol%) at different temperatures.

### B. Angle $\theta$ and poling period $\Lambda$ for type-I and type-0 phase-matching conditions

It is also possible to prepare spectrally pure states under the type I and type-0 phase-matching conditions, as long as the angle  $\theta$  is between  $0^\circ$  and  $90^\circ$ . Type-0 and type-I PDC in PPLN are routinely used in many quantum optics experiments, e.g., in biphoton states generation and frequency conversion [46, 47]. Figure 3(a-c) shows the angle  $\theta$  as a function of the pump and the signal wavelengths under type-I ( $e \rightarrow o+o$ ) phase-matching condition. The pump wavelength is in the range of 300-900 nm and the signal is in the range of 500-5000 nm. Figure 3(d-f) shows the corresponding poling period  $\Lambda$ , ranging from  $9.3 \mu\text{m}$  to  $79.0 \mu\text{m}$ . For wavelengths near the degenerated case, the poling period is larger than the case of far from the degenerated condition. The  $\Lambda$  of InZnLN is larger than the values of MgLN and ZnLN.

Figure 4(a-c) shows the case for type-0 ( $e \rightarrow e+e$ ) phase-matching condition. The pump wavelength is in the range of 600-1500 nm, and the signal is in the range of 700-5000 nm. The corresponding poling period  $\Lambda$  is between  $13.6 \mu\text{m}$  to  $27.7 \mu\text{m}$ , as shown in Fig. 4(d-f). The three crystals have a similar performance under the type-0 phase matching-condition.

Crystal Name	MgLN	ZnLN	InZnLN
$\lambda_{\text{GVM1}}$ at $20^\circ\text{C}$ (nm)	2474.6	2483.7	2450.7
$\Delta\lambda_{\text{GVM1}}$ 20-120 °C (nm)	-2.8	-2.8	-2.8
$\lambda_{\text{GVM2}}$ at $20^\circ\text{C}$ (nm)	4019.7	4002.5	3557.3
$\Delta\lambda_{\text{GVM2}}$ 20-120 °C (nm)	75.9	78.1	87.3
$\lambda_{\text{GVM3}}$ at $20^\circ\text{C}$ (nm)	3209.3	3203.8	2960.2
$\Delta\lambda_{\text{GVM3}}$ 20-120 °C (nm)	39.7	40.5	41.1
$\Lambda_{\text{GVM1}}$ at $20^\circ\text{C}$ ( $\mu\text{m}$ )	14.1	14.2	16.6
$\Lambda_{\text{GVM2}}$ at $20^\circ\text{C}$ ( $\mu\text{m}$ )	14.4	14.5	16.7
$\Lambda_{\text{GVM3}}$ at $20^\circ\text{C}$ ( $\mu\text{m}$ )	15.0	15.1	17.2
References	[43]	[44]	[45]

TABLE II. Comparison of the GVM wavelengths  $\lambda_{\text{GVM1}(2,3)}$  at  $20^\circ\text{C}$ , the wavelength difference  $\Delta\lambda_{\text{GVM1}(2,3)}$  between  $20^\circ\text{C}$  and  $120^\circ\text{C}$ , and the poling period  $\Lambda_{\text{GVM1}(2,3)}$  under three GVM conditions for three doped LN crystals: Mg(5 mol%)LN, Zn(5 mol%)LN and In(5 mol%)Zn(5.5 mol%)LN.

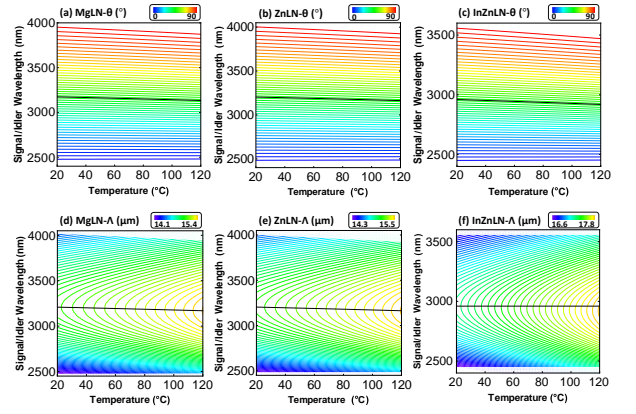


FIG. 6. (a-c): The tilt angle  $\theta$  as functions of signal (idler) wavelength and temperature for crystals with fixed doping ratio, i.e., MgLN [ $\text{MgO}(5 \text{ mol\%})\text{:LiNbO}_3$ ], ZnLN [ $\text{ZnO}(5 \text{ mol\%})\text{:LiNbO}_3$ ], and InZnLN [ $\text{In}_2\text{O}_3(5 \text{ mol\%})\text{:ZnO}(5.5 \text{ mol\%})\text{:LiNbO}_3$ ]. (d-f): The corresponding poling period. In these figures, the signal and the idler photons have the degenerated wavelengths under **type-II** phase-matching condition. The solid black line indicates  $\theta = 45^\circ$ , and the dashed black line indicates  $\lambda_s = 2\lambda_p$ .

### C. Thermal properties

In this subsection, we investigate the thermal properties of the doped PPLN crystals. Temperature is a crucial parameter for quasi-phase-matched (QPM) crystals, since the phase-matching conditions in the QPM crystals are mainly controlled by temperature in the experiments. Using the temperature-dependent Sellmeier equations in Refs. [43–45], we can calculate the GVM wavelength as a function of the temperature. We first consider the case of MgLN with different doping ratios, and then we compare MgLN with ZnLN and InZnLN at a fixed doping ratio. Figure 5(a) shows the case of GVM<sub>1</sub> wavelength, which increases linearly with the increase of temperature. When the temperature increases from  $20^\circ\text{C}$  to  $120^\circ\text{C}$ , the GVM wavelength increases by about 2.8 nm for all the doping ratio from 0 to 7 mol%. Figure 5(b) and (c) show the cases of GVM<sub>2</sub> and GVM<sub>3</sub> wavelengths, which decrease by about 78 nm and 40 nm respectively when the temperature increases from  $20^\circ\text{C}$  to  $120^\circ\text{C}$ . By comparing Figs. 5(a), (b), and (c), it can be concluded that the GVM<sub>2</sub> wavelength is the most sensitive one to the temperature increase, i.e., decreases by about 78 nm. In contrast, GVM<sub>1</sub> is not so sensitive, i.e., only increase by 2.8 nm.

Next, we consider the thermal properties of other doped LN crystals. We compare the case of Mg(5 mol%)LN, Zn(5 mol%)LN, and In(5 mol%)Zn(5.5 mol%)LN in Fig. 6 and Tab. II. The most apparent feature in Fig. 6 and Tab. II is that the signal/idler wavelength changes linearly. The wavelength difference between  $20^\circ\text{C}$  and  $120^\circ\text{C}$ ,  $\Delta\lambda_{\text{GVM}}$ , is almost the same for three different crystals, i.e.,  $\Delta\lambda_{\text{GVM1}}$ ,  $\Delta\lambda_{\text{GVM2}}$ , and

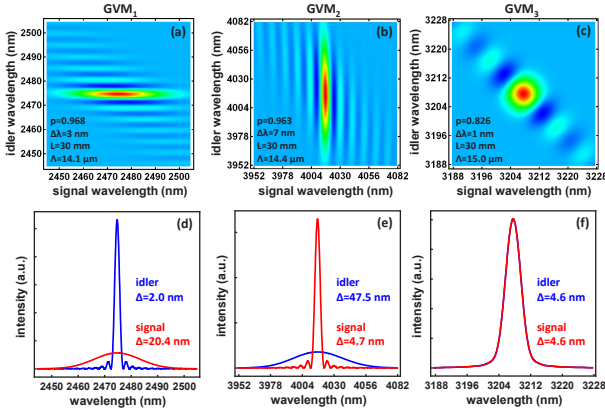
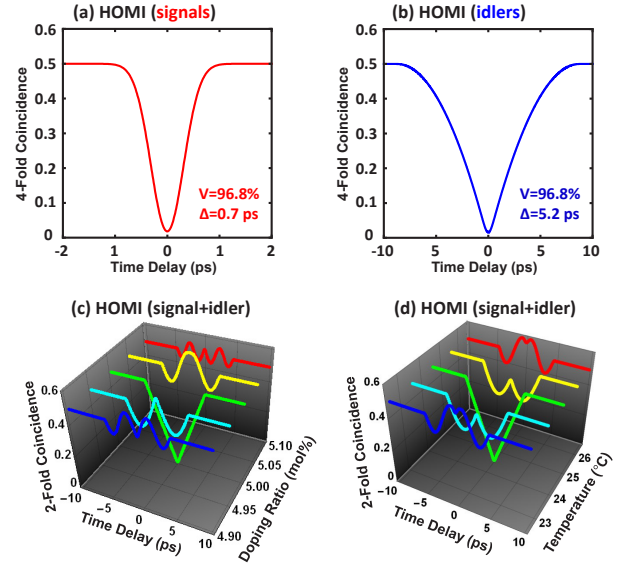


FIG. 7. The JSA and spectra of biphotons generated from 5 mol% MgO doped PPLN under GVM<sub>1</sub>, GVM<sub>2</sub>, and GVM<sub>3</sub> conditions. The purity  $p$ , the pump bandwidth  $\Delta\lambda$ , the crystal length  $L$ , the poling period  $\Lambda$ , and FWHM values ( $\Delta$ ) are listed in the figure. Note the blue curve and red curve are overlapped in (f).

$\Delta\lambda_{\text{GVM}_3}$  are about 2.8 nm, 78 nm, and 40 nm, respectively. This phenomenon implies that the thermal-related GVM wavelength is not dominated by the doped elements, but by the main component, LiNbO<sub>3</sub>. The calculated the poling period of the three crystals at 20 °C are in the range of 14-15  $\mu\text{m}$ , which can be realized with the current technology. Note that the thermal expansion of the LN crystals are not considered in the calculation, since such data are not available in the references.

#### D. Hong-Ou-Mandel interference

In this subsection, we consider the possible future applications of the spectrally-uncorrelated biphotons in Hong-Ou-Mandel interference [48, 49], which is the foundation for many QIP applications such as quantum computation [19], boson sampling [20], and quantum teleportation [21]. Figure 7 shows the JSA of the biphotons generated from 5 mol% MgO doped PPLN under GVM<sub>1</sub>, GVM<sub>2</sub>, and GVM<sub>3</sub> conditions. The spectral ranges for Figs. 7(a-c) are 60 nm, 130 nm, and 40 nm, respectively. The dimension of each JSA matrix is  $200 \times 200$ . Note the photon bandwidths shown in Fig. 7 are just examples. In fact, the bandwidth is strongly dependent on the pulse duration and the crystal length, and the same photon purity can be achieved at different combinations of pump pulse and crystal length. The biphotons under GVM<sub>1</sub> and GVM<sub>2</sub> conditions (see Fig. 7(a, b)) can be used for HOM interference between two independent sources, with a typical experimental setup shown in Refs. [14, 50]. In the experiment, two signals  $s_1$  and  $s_2$  are sent to a beamsplitter for interference and then detected by two single-photon detectors, while two idlers  $i_1$  and  $i_2$  are directly sent to single-photon detectors for heralding the signals. The four-fold coincidence probability  $P_4$



function of  $\tau$  is given by [51–53]:

$$P_2(\tau) = \frac{1}{4} \int_0^\infty \int_0^\infty d\omega_s d\omega_i \left| [f(\omega_s, \omega_i) - f(\omega_i, \omega_s) e^{-i(\omega_s - \omega_i)\tau}] \right|^2. \quad (14)$$

The green curve in Fig. 8(c) is the simulated HOM interference pattern between a signal and an idler from the same Mg(5 mol%)LN crystal at 24.5°C, with the JSA shown in Fig. 8(c). Under this condition, the visibility is as high as 100%. By fixing the poling period and changing the doping ratio to 4.90 mol%, 4.95 mol%, 5.05 mol%, and 5.10 mol%, the interference patterns oscillate, as shown in Fig. 8(c). By changing the temperature to 22.5°C, 23.5°C, 25.5°C and 26.5°C, the interference patterns also oscillate, as shown in Fig. 8(d).

#### IV. DISCUSSIONS

We notice that LN crystal has several different growing methods, and each method has a different effect on the Sellmeier equations. The MgLN, ZnLN, and InZnLN crystals investigated in the Calculation and Simulation section were grown using the Czochralski technique from a congruent melt (mole ratio Li/Nb  $\approx$  0.942) [43–45]. As shown in Fig. 1, 0 mol% Zn doped LN (i.e., pure LN) has the GVM<sub>1</sub>, GVM<sub>2</sub>, GVM<sub>3</sub> wavelengths of 2478.6 nm, 3931.4 nm, and 3163.6 nm, respectively. In contrast, the pure LN grown from the stoichiometric melt (mole ratio Li/Nb  $\approx$  1) [54] has the GVM<sub>1</sub>, GVM<sub>2</sub>, GVM<sub>3</sub> wavelengths of 2681.0 nm, 4653.6 nm, and 3595.8 nm, respectively. Further, using the Sellmeier equations from Ref. [55], the pure LN grown from the congruent melt (mole ratio Li/Nb  $\approx$  0.937) has the GVM<sub>1</sub>, GVM<sub>2</sub>, GVM<sub>3</sub> wavelengths of 2678.5 nm, 4361.7 nm, and 3499.1 nm, respectively. These differences are mainly caused by different growing methods. In addition, the LN crystal can also be doped with other elements, which also affect the Sellmeier equations. For example, NdMgLN crystal (grown by the Czochralski technique from a congruent melt in Ref. [56] has the GVM<sub>1</sub>, GVM<sub>2</sub>, GVM<sub>3</sub> wavelengths of 2615.3 nm, 4562.5 nm, and 3511.5 nm, respectively. We also investigated ErMgLN and MgTiLN crystal [57, 58]. However, they do not satisfy the three kinds of GVM conditions. In this calculation, the maximal doping ratio we considered is 7 mol%. In fact, this ratio can still be improved, and we anticipate the wavelength tunability can be further improved at a larger doping ratio.

In this work, limited by the available Sellmeier equations, we only investigate the LN crystals doped with Mg, Zn, In, and Nd. In the future, it is promising to explore more LN crystals doped with different chemical elements and with different doping ratios. Another promising direction is investigating the spectrally pure single-photon state generation from doped PPLN waveguide [59–61] or doped PPLN film [62], which has the

merits of higher nonlinear efficiency, easier for integration and microminiaturization. In Fig. 7, the purities are 0.968, 0.963, and 0.826, respectively, and this purity can be further improved to near 1 using the custom poling technique [63, 64].

In the section of Calculation and Simulation, we only show the configuration of  $o \rightarrow o + e$  in the type-II phase-matching condition. In fact, we also investigate the configuration of  $e \rightarrow o + e$ . Although the GVM<sub>2</sub> wavelength under this configuration is in the telecom wavelength, the effective nonlinear coefficient, unfortunately, is zero. The reason is analyzed in detail in the Appendix.

For future applications, spectrally uncorrelated biphotons can be used to prepare pure single-photons and entangled photons which can be applied for sensing, imaging, and communication with a quantum-enhanced performance at MIR region. As shown in the section of Calculation and simulation, all the poling periods of the doped PPLN crystals are above 5  $\mu$ m, which can be easily fabricated using the off-the-shelf technology. So, the MIR-band single-photon source calculated in the work is ready for fundamental research and industry applications, so as to promote the second quantum revolution.

#### V. CONCLUSION

In conclusion, we have theoretically studied the preparation of spectrally uncorrelated biphotons at MIR wavelengths from doped LN crystals, including MgO doped LN, ZnO doped LN, and In<sub>2</sub>O<sub>3</sub> doped ZnLN with doping ratio from 0 to 7 mol%. The tilt angle, poling period, thermal properties, and HOM interference of the biphotons are calculated under type-II, type-I, and type-0 phase-matching conditions. For 5 mol% MgO doped LN, the three GVM wavelengths are 2474.7 nm, 4016.6 nm, and 3207.6 nm, and the corresponding purities are 0.968, 0.963, and 0.826, respectively. In the calculation of the thermal properties, we found that thermal-related GVM wavelength is not dominated by the doped elements, but by LiNbO<sub>3</sub>. When the temperature was increased from 20 °C to 120 °C, the three GVM wavelengths are increased by about 2.8 nm, -78 nm, and -40 nm, respectively. In the simulation of HOM interference using the 5 mol% MgO doped PPLN, visibility of 96.8% was achieved in a HOM interference between two independent sources, and visibility of 100% was achieved in a HOM interference between the signal and idler from the same SPDC source. The interference patterns oscillate by changing the doping ratio or temperature. The spectrally uncorrelated biphotons can be used to prepare pure single-photon source and entangled photon source at MIR wavelengths.

## ACKNOWLEDGMENTS

This work is partially supported by the National Key R&D Program of China (Grant No. 2018YFA0307400), the National Natural Science Foundations of China (Grant Nos. 91836102, 11704290, 12074299, 61775025, 61405030), and the Program of State Key Laboratory of Quantum Optics and Quantum Optics Devices (No: KF201813). We thank Profs. Zhi-Yuan Zhou, Yan-Xiao Gong, and Ping Xu for helpful discussions.

## APPENDIX : THE EFFECTIVE NONLINEAR COEFFICIENT

The effective nonlinear coefficient  $d_{\text{eff}}$  for collinear phase-matching in uniaxial crystals can be deduced as follow [65].

For  $o \rightarrow o + e$  phase-matching condition,

$$\begin{aligned} d_{\text{eff}}(\text{ooe}) = & -d_{xxx}C_\theta C_\phi S_\phi^2 + d_{xyy}C_\theta C_\phi S_\phi^2 - d_{xyz}S_\theta C_\phi S_\phi \\ & + d_{xxz}S_\theta S_\phi^2 + d_{xxy}(C_\theta C_\phi^2 S_\phi - C_\theta S_\phi^3) \\ & + d_{yxx}C_\theta C_\phi^2 S_\phi - d_{yyy}C_\theta C_\phi^2 S_\phi + d_{yyz}S_\theta C_\phi C_\phi^2 \\ & - d_{yxz}S_\theta C_\phi S_\phi + d_{yxy}(C_\theta C_\phi S_\phi^2 - C_\theta C_\phi^3). \end{aligned} \quad (15)$$

For  $e \rightarrow o + e$  phase-matching condition,

$$\begin{aligned} d_{\text{eff}}(\text{eoe}) = & d_{xxx}C_\theta^2 C_\phi^2 S_\phi - d_{xyy}C_\theta^2 C_\phi^2 S_\phi + d_{xyz}C_\theta S_\theta C_\phi^2 \\ & - d_{xxz}C_\theta S_\theta C_\phi S_\phi + d_{xxy}(C_\theta^2 C_\phi S_\phi^2 - C_\theta^2 C_\phi^3) \\ & + d_{yxx}C_\theta^2 C_\phi S_\phi^2 - d_{yyy}C_\theta^2 C_\phi S_\phi^2 + d_{yyz}C_\theta S_\theta C_\phi S_\phi \\ & - d_{yxz}C_\theta S_\theta S_\phi^2 + d_{yxy}(C_\theta^2 S_\phi^3 - C_\theta^2 C_\phi^2 S_\phi) \\ & - d_{zxx}C_\theta S_\theta C_\phi S_\phi + d_{zyy}C_\theta S_\theta C_\phi S_\phi - d_{zyz}S_\theta^2 C_\phi \\ & + d_{zxx}S_\theta^2 S_\phi + d_{zxy}(C_\theta S_\theta C_\phi^2 - C_\theta S_\theta S_\phi^2), \end{aligned} \quad (16)$$

where  $S_\theta = \sin(\theta + \rho)$ ,  $C_\theta = \cos(\theta + \rho)$ ,  $S_\phi = \sin \phi$ ,  $C_\phi = \cos \phi$ , and  $\rho$  is the walk-off angle.  $\theta$  is the polar angle,  $\phi$  is the azimuth angle, and Z is the optical axis, as defined in Fig.9(a). For PPLN under  $o \rightarrow o + e$  or  $e \rightarrow o + e$  phase-matching conditions,  $\rho = 0^\circ$ ,  $\theta = 90^\circ$ ,

and  $\phi = 90^\circ$ , as shown in Fig.9(b, c). Therefore,

$$d_{\text{eff}}(\text{ooe}) = d_{xxz} \quad (17)$$

and

$$d_{\text{eff}}(\text{eoe}) = d_{zxx}. \quad (18)$$

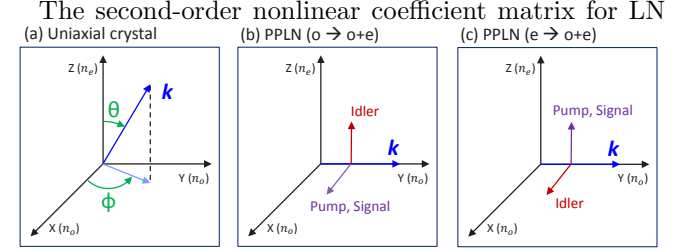


FIG. 9. (a) The general refractive index coordinates for uniaxial crystals. (b, c) The refractive index coordinate for PPLN crystal under ( $o \rightarrow o + e$ ) or ( $e \rightarrow o + e$ ) type-II phase-matching condition.

is [66]:

$$\begin{aligned} d &= \begin{pmatrix} 0 & 0 & 0 & 0 & d_{xxz} & d_{xxy} \\ d_{yxx} & d_{yyy} & 0 & d_{yyz} & 0 & 0 \\ d_{zxx} & d_{zyy} & d_{zzz} & 0 & 0 & 0 \end{pmatrix} \\ &= \begin{pmatrix} 0 & 0 & 0 & 0 & d_{15} & d_{16} \\ d_{21} & d_{22} & 0 & d_{24} & 0 & 0 \\ d_{31} & d_{32} & d_{33} & 0 & 0 & 0 \end{pmatrix} \\ &= \begin{pmatrix} 0 & 0 & 0 & 0 & -4.6 & -2.2 \\ -2.2 & 2.2 & 0 & -4.6 & 0 & 0 \\ -4.6 & -4.6 & -25.0 & 0 & 0 & 0 \end{pmatrix}. \end{aligned} \quad (19)$$

So,

$$d_{\text{eff}}(\text{ooe}) = d_{xxz} = -4.6 \text{ pm/V} \quad (20)$$

and

$$d_{\text{eff}}(\text{eoe}) = d_{zxx} = 0. \quad (21)$$

Therefore, the configuration of  $e \rightarrow o + e$  does not exist for PPLN.

- [1] Eric Tournie and Laurent Cerutti, eds., *Mid-infrared optoelectronics materials, devices, and applications* (Woodhead Publishing, 2019).
- [2] Majid Ebrahim-Zadeh and Irina T. Sorokina, eds., *Mid-Infrared Coherent Sources and Applications* (Springer Science & Business Media, 2008).
- [3] Raghi S. El Shamy, Diaa Khalil, and Mohamed A. Swillam, "Mid infrared optical gas sensor using plasmonic Mach-Zehnder interferometer," *Sci. Rep.* **10**, 1–9 (2020).

- [4] Ke Chen, Shuai Liu, Bo Zhang, Zhenfeng Gong, Yewei Chen, Ming Zhang, Hong Deng, Min Guo, Fengxiang Ma, and Feng Zhu, "Highly sensitive photoacoustic multi-gas analyzer combined with mid-infrared broadband source and near-infrared laser," *Opt. Lasers Eng.* **124**, 105844 (2020).
- [5] Francesco Bellei, Alyssa P. Cartwright, Adam N. McCaughan, Andrew E. Dane, Faraz Najafi, Qingyuan Zhao, and Karl K. Berggren, "Free-space-coupled su-

- perconducting nanowire single-photon detectors for infrared optical communications,” *Opt. Express* **24**, 3248–3257 (2016).
- [6] Andreas Tittel, Ann-Katrin U Michel, Martin Schäferling, Xinghui Yin, Behrad Gholipour, Long Cui, Matthias Wuttig, Thomas Taubner, Frank Neubrech, and Harald Giessen, “A switchable mid-infrared plasmonic perfect absorber with multispectral thermal imaging capability,” *Adv. Mater.* **27**, 4597–4603 (2015).
- [7] M. Mancinelli, A. Trenti, S. Piccione, G. Fontana, J. S. Dam, P. Tidemand-Lichtenberg, C. Pedersen, and L. Pavesi, “Mid-infrared coincidence measurements on twin photons at room temperature,” *Nat. Commun.* **8**, 15184 (2017).
- [8] Richard Soref, “Enabling 2  $\mu\text{m}$  communications,” *Nat. Photon.* **9**, 358–359 (2015).
- [9] Kwang Jo Lee, Sunmi Lee, and Heedeuk Shin, “Extended phase-matching properties of periodically poled potassium niobate crystals for mid-infrared polarization-entangled photon-pair generation,” *Appl. Opt.* **55**, 9791–9796 (2016).
- [10] Richard A. McCracken, Francesco Graffitti, and Alessandro Fedrizzi, “Numerical investigation of mid-infrared single-photon generation,” *J. Opt. Soc. Am. B* **35**, C38–C48 (2018).
- [11] Lawrence M. Rosenfeld, Dominic A. Sulway, Gary F. Sinclair, Vikas Anant, Mark G. Thompson, John G. Rarity, and Joshua W. Silverstone, “Mid-infrared quantum optics in silicon,” arXiv: 1906.10158.
- [12] Dmytro Kundys, Francesco Graffitti, Richard A. McCracken, Alessandro Fedrizzi, and Bohdan Kundys, “Numerical study of reconfigurable Mid-IR single photon sources based on functional ferroelectrics,” *Adv. Quantum Technol.*, 1900092 (2020).
- [13] Shashi Prabhakar, Taylor Shields, Adetunmise C. Dada, Mehdi Ebrahim, Gregor G. Taylor, Dmitry Morozov, Kleantlis Erotokritou, Shigehito Miki, Masahiro Yabuno, Hirotaka Terai, Corin Gawith, Michael Kues, Lucia Caspani, Robert H. Hadfield, and Matteo Clerici, “Two-photon quantum interference and entanglement at 2.1  $\mu\text{m}$ ,” *Sci. Adv.* **6**, eaay5195 (2020).
- [14] Peter J. Mosley, Jeff S. Lundeen, Brian J. Smith, Piotr Wasylczyk, Alfred B. U’Ren, Christine Silberhorn, and Ian A. Walmsley, “Heralded generation of ultrafast single photons in pure quantum states,” *Phys. Rev. Lett.* **100**, 133601 (2008).
- [15] W. P. Grice, A. B. U’Ren, and I. A. Walmsley, “Eliminating frequency and space-time correlations in multiphoton states,” *Phys. Rev. A* **64**, 063815 (2001).
- [16] Alfred B. U’Ren, Christine Silberhorn, Reinhard Erdmann, Konrad Banaszek, Warren P. Grice, Ian A. Walmsley, and Michael G. Raymer, “Generation of pure-state single-photon wavepackets by conditional preparation based on spontaneous parametric downconversion,” arXiv: quant-ph/0611019 (2006).
- [17] Francesco Graffitti, Jeremy Kelly-Massicotte, Alessandro Fedrizzi, and Agata M. Branczyk, “Design considerations for high-purity heralded single-photon sources,” *Phys. Rev. A* **98**, 053811 (2018).
- [18] Fabian Laudenbach, Hannes Hubel, Michael Hentschel, Philip Walther, and Andreas Poppe, “Modelling parametric down-conversion yielding spectrally pure photon pairs,” *Opt. Express* **24**, 2712–2727 (2016).
- [19] Ian A. Walmsley and Michael G. Raymer, “Toward quantum-information processing with photons,” *Science* **307**, 1733 (2005).
- [20] Matthew A. Broome, Alessandro Fedrizzi, Saleh Rahimi-Keshari, Justin Dove, Scott Aaronson, Timothy C. Ralph, and Andrew G. White, “Photonic boson sampling in a tunable circuit,” *Science* **339**, 794 (2013).
- [21] Raju Valivarthi, Marcel Li Grimau Puigibert, Qiang Zhou, Gabriel H. Aguilar, Varun B. Verma, Francesco Marsili, Matthew D. Shaw, Sae Woo Nam, Daniel Oblak, and Wolfgang Tittel, “Quantum teleportation across a metropolitan fibre network,” *Nat. Photon.* **10**, 676 (2016).
- [22] Raju Valivarthi, Qiang Zhou, Caleb John, Francesco Marsili, Varun B Verma, Matthew D Shaw, Sae Woo Nam, Daniel Oblak, and Wolfgang Tittel, “A cost-effective measurement-device-independent quantum key distribution system for quantum networks,” *Quantum Sci. Technol.* **2**, 04LT01 (2017).
- [23] Tomohisa Nagata, Ryo Okamoto, Jeremy L. O’Brien, Keiji Sasaki, and Shigeki Takeuchi, “Beating the standard quantum limit with four-entangled photons,” *Science* **316**, 726–729 (2007).
- [24] Masahiro Yabuno, Ryosuke Shimizu, Yasuyoshi Mitsumori, Hideo Kosaka, and Keiichi Edamatsu, “Four-photon quantum interferometry at a telecom wavelength,” *Phys. Rev. A* **86**, 010302 (2012).
- [25] David N Nikogosyan, *Nonlinear optical crystals: a complete survey* (Springer Science & Business Media, 2005).
- [26] Shi-Long Liu, Shi-Kai Liu, Yin-Hai Li, Shuai Shi, Zhi-Yuan Zhou, and Bao-Sen Shi, “Coherent frequency bridge between visible and telecommunications band for vortex light,” *Opt. Express* **25**, 24290–24298 (2017).
- [27] Chen Yang, Shi-Long Liu, Zhi-Yuan Zhou, Yan Li, Yin-Hai Li, Shi-Kai Liu, Zhao-Huai Xu, Guang-Can Guo, and Bao-Sen Shi, “Extra-cavity-enhanced difference-frequency generation at 1.63  $\mu\text{m}$ ,” *J. Opt. Soc. Am. B* **37**, 1367–1371 (2020).
- [28] TianXin Wang, PengCheng Chen, Chuan Xu, Yong Zhang, DunZhao Wei, XiaoPeng Hu, Gang Zhao, Min Xiao, and ShiNing Zhu, “Periodically poled LiNbO<sub>3</sub> crystals from 1D and 2D to 3D,” *Sci. China Technol. Sci.*, s11431-019-1503-0 (2020).
- [29] Rui-Bo Jin, Takuma Saito, and Ryosuke Shimizu, “Time-frequency duality of biphotons for quantum optical synthesis,” *Phys. Rev. Applied* **10**, 034011 (2018).
- [30] Yongfa Kong, Fang Bo, Weiwei Wang, Dahuai Zheng, Hongde Liu, Guoquan Zhang, Romano Rupp, and Jingjun Xu, “Recent progress in lithium niobate: Optical damage, defect simulation, and on-chip devices,” *Adv. Mater.* **32**, 1806452 (2020).
- [31] F. Abdi, M. Aillerie, M. Fontana, P. Bourson, T. Volk, B. Maximov, S. Sulyanov, N. Rubinina, and M. Wohlecke, “Influence of Zn doping on electrooptical properties and structure parameters of lithium niobate crystals,” *Appl. Phys. B* **68**, 795–799 (1999).
- [32] Guoquan Zhang, Guangyin Zhang, Simin Liu, Jingjun Xu, Qian Sun, and Xinzheng Zhang, “The threshold effect of incident light intensity for the photorefractive light-induced scattering in LiNbO<sub>3</sub>:Fe,M (M=Mg<sup>2+</sup>, Zn<sup>2+</sup>, In<sup>3+</sup>) crystals,” *J. Appl. Phys.* **83**, 4392–4396 (1998).
- [33] M.N. Palatnikov, I.V. Biryukova, N.V. Sidorov, A.V. Denisov, V.T. Kalinnikov, P.G.R. Smith, and V.Ya. Shur, “Growth and concentration dependencies of rare-

- earth doped lithium niobate single crystals,” *J. Cryst. Growth* **291**, 390–397 (2006).
- [34] Subhojit Dutta, Elizabeth A. Goldschmidt, Sabyasachi Barik, Uday Saha, and Edo Waks, “Integrated photonic platform for rare-earth ions in thin film lithium niobate,” *Nano Lett.* **20**, 741–747 (2020).
- [35] P J Mosley, J S Lundeen, B J Smith, and I A Walmesley, “Conditional preparation of single photons using parametric downconversion: a recipe for purity,” *New J. Phys.* **10**, 093011 (2008).
- [36] Rui-Bo Jin, Ryosuke Shimizu, Kentaro Wakui, Hugo Benichi, and Masahide Sasaki, “Widely tunable single photon source with high purity at telecom wavelength,” *Opt. Express* **21**, 10659–10666 (2013).
- [37] Keiichi Edamatsu, Ryosuke Shimizu, Wakana Ueno, Rui-Bo Jin, Fumihiko Kaneda, Masahiro Yabuno, Hirofumi Suzuki, Shigehiro Nagano, Atsushi Syouji, and Koji Suizu, “Photon pair sources with controlled frequency correlation,” *Prog. Inform.* **8**, 19–26 (2011).
- [38] Rui-Bo Jin, Neng Cai, Ying Huang, Xiang-Ying Hao, Shun Wang, Fang Li, Hai-Zhi Song, Qiang Zhou, and Ryosuke Shimizu, “Theoretical investigation of a spectrally pure-state generation from isomorphs of KDP crystal at near-infrared and telecom wavelengths,” *Phys. Rev. Appl.* **11**, 034067 (2019).
- [39] Nicolas Quesada and Agata M. Brańczyk, “Gaussian functions are optimal for waveguided nonlinear-quantum-optical processes,” *Phys. Rev. A* **98**, 043813 (2018).
- [40] Rui-Bo Jin, Wu-Hao Cai, Chunling Ding, Feng Mei, Guang-Wei Deng, Ryosuke Shimizu, and Qiang Zhou, “Spectrally uncorrelated biphotons generated from the family of BBO crystal,” *Quantum Engineering* **2**, e38 (2020).
- [41] Wu-Hao Cai, Bei Wei, Shun Wang, and Rui-Bo Jin, “Counter-propagating spectrally uncorrelated biphotons at 1550 nm generated from periodically poled  $MTiOXO_4$  ( $M=K, Rb, Cs; X=P, As$ ),” *J. Opt. Soc. Am. B* **37**, 3048–3054 (2020).
- [42] Jia-Chen Duan, Ji-Ning Zhang, Yin-Jun Zhu, Chang-Wei Sun, Yi-Chen Liu, Ping Xu, Zhenda Xie, Yan-Xiao Gong, and Shi-Ning Zhu, “Generation of narrowband counterpropagating polarization-entangled photon pairs based on thin-film lithium niobate on insulator,” *J. Opt. Soc. Am. B* **37**, 2139–2145 (2020).
- [43] U. Schlarb and K. Betzler, “Influence of the defect structure on the refractive indices of undoped and Mg-doped lithium niobate,” *Phys. Rev. B* **50**, 751–757 (1994).
- [44] U. Schlarb, M. W hlecke, B. Gather, A. Reichert, K. Betzler, T. Volk, and N. Rubina, “Refractive indices of Zn-doped lithium niobate,” *Opt. Mater.* **4**, 791–795 (1995).
- [45] U. Schlarb, B. Matzas, A. Reichert, K. Betzler, M. W hlecke, B. Gather, and T. Volk, “Refractive indices of Zn/In-co-doped lithium niobate,” *Ferroelectrics* **185**, 269–272 (1996).
- [46] B. Brecht, Dileep V. Reddy, C. Silberhorn, and M. G. Raymer, “Photon temporal modes: A complete framework for quantum information science,” *Phys. Rev. X* **5**, 041017 (2015).
- [47] Vahid Ansari, John M. Donohue, Benjamin Brecht, and Christine Silberhorn, “Tailoring nonlinear processes for quantum optics with pulsed temporal-mode encodings,” *Optica* **5**, 534–550 (2018).
- [48] C. K. Hong, Z. Y. Ou, and L. Mandel, “Measurement of subpicosecond time intervals between two photons by interference,” *Phys. Rev. Lett.* **59**, 2044–2046 (1987).
- [49] Agata M. Brańczyk, “Hong-Ou-Mandel Interference,” arXiv: 1711.00080 (2017).
- [50] Rui-Bo Jin, Kentaro Wakui, Ryosuke Shimizu, Hugo Benichi, Shigehito Miki, Taro Yamashita, Hiroataka Terai, Zhen Wang, Mikio Fujiwara, and Masahide Sasaki, “Nonclassical interference between independent intrinsically pure single photons at telecommunication wavelength,” *Phys. Rev. A* **87**, 063801 (2013).
- [51] Zhe-Yu Jeff Ou, *Multi-photon quantum interference* (Springer, 2007).
- [52] Rui-Bo Jin, Thomas Gerrits, Mikio Fujiwara, Ryota Wakabayashi, Taro Yamashita, Shigehito Miki, Hiroataka Terai, Ryosuke Shimizu, Masahiro Takeoka, and Masahide Sasaki, “Spectrally resolved Hong-Ou-Mandel interference between independent photon sources,” *Opt. Express* **23**, 28836–28848 (2015).
- [53] I. A. Grice, W. P. & Walmsley, “Spectral information and distinguishability in type-II down-conversion with a broadband pump,” *Phys. Rev. A* **56**, 1627–1634 (1997).
- [54] M. V. Hobden and J. Warner, “The temperature dependence of the refractive indices of pure lithium niobate,” *Phys. Lett* **22**, 243–244 (1966).
- [55] David E. Zelmon, David L. Small, and Dieter Jundt, “Infrared corrected Sellmeier coefficients for congruently grown lithium niobate and 5 mol.% magnesium oxide-doped lithium niobate,” *J. Opt. Soc. Am. B* **14**, 3319–3322 (1997).
- [56] G. K. Kitaeva, I.I. Naumova, A.A. Mikhailovsky, P.S. Losevsky, and A.N. Penin, “Visible and infrared dispersion of the refractive indices in periodically poled and single domain Nd:Mg:LiNbO<sub>3</sub> crystals,” *Appl. Phys. B* **66**, 201–205 (1998).
- [57] De-Long Zhang, Qing-Zhong Yang, Ping-Rang Hua, Hong-Li Liu, Yu-Ming Cui, Liang Sun, Yu-Heng Xu, and Edwin Yue-Bun Pun, “Sellmeier equation for doubly Er/Mg-doped congruent LiNbO<sub>3</sub> crystals,” *J. Opt. Soc. Am. B* **26**, 620–626 (2009).
- [58] Chang Yongmao, Wen Jinke, Wang Huafu, and Li Bing, “Refractive index measurement and second harmonic generation in a series of LiNbO<sub>3</sub>: Mg (5 mol%) crystals,” *Chin. Phys. Lett.* **9**, 427 (1992).
- [59] Xiang Cheng, Murat Can Sarihan, Kai-Chi Chang, Yoo Seung Lee, Fabian Laudenbach, Han Ye, Zhongyuan Yu, and Chee Wei Wong, “Design of spontaneous parametric down-conversion in integrated hybrid Si<sub>x</sub>N<sub>y</sub>-PPLN waveguides,” *Opt. Express* **27**, 30773–30787 (2019).
- [60] Chang-Wei Sun, Su-Heng Wu, Jia-Chen Duan, Jian-Wei Zhou, Jun-Lei Xia, Ping Xu, Zhenda Xie, Yan-Xiao Gong, and Shi-Ning Zhu, “Compact polarization-entangled photon-pair source based on a dual-periodically-poled Ti:LiNbO<sub>3</sub> waveguide,” *Opt. Lett.* **44**, 5598–5601 (2019).
- [61] Yunfei Niu, Chen Lin, Xiaoyue Liu, Yan Chen, Xiaopeng Hu, Yong Zhang, Xinlun Cai, Yan-Xiao Gong, Zhenda Xie, and Shining Zhu, “Optimizing the efficiency of a periodically poled LNOI waveguide using in situ monitoring of the ferroelectric domains,” *Appl. Phys. Lett.* **116**, 101104 (2020).
- [62] Licheng Ge, Yuping Chen, Haowei Jiang, Guangzhen Li, Bing Zhu, Yi’an Liu, and Xianfeng Chen, “Broadband quasi-phase matching in a MgO:PPLN thin film,” *Photon. Res.* **6**, 954–958 (2018).

- [63] Agata M. Brańczyk, Alessandro Fedrizzi, Thomas M. Stace, Tim C. Ralph, and Andrew G. White, “Engineered optical nonlinearity for quantum light sources,” *Opt. Express* **19**, 55–65 (2011).
- [64] Chaohan Cui, Reeshad Arian, Saikat Guha, N. Peyghambarian, Quntao Zhuang, and Zheshen Zhang, “Wavefunction engineering for spectrally uncorrelated biphotons in the telecommunication band based on a machine-learning framework,” *Phys. Rev. Appl.* **12**, 034059 (2019).
- [65] Arlee Smith, *Crystal nonlinear optics with SNLO examples* (AS-Photonics, 2016).
- [66] A. Smith, “Snlo,” <http://www.as-photonics.com/snlo>.